Universiteit Leiden
The Netherlands

Insights into the mechanism of electrocatalytic CO2 reduction and concomitant catalyst degradation pathways

Raaijman, S.J.

Citation

Raaijman, S. J. (2022, January 19). *Insights into the mechanism of electrocatalytic CO2 reduction and concomitant catalyst degradation pathways*. Retrieved from https://hdl.handle.net/1887/3250500

Version:	Publisher's Version
License:	Licence agreement concerning inclusion of doctoral thesis in the Institutional Repository of the University of Leiden
Downloaded from:	https://hdl.handle.net/1887/3250500

Note: To cite this publication please use the final published version (if applicable).

3

Anisotropic Cathodic Corrosion of Gold Electrodes in Absence and Presence of CO

In this work, we investigate gold surface dissolution under cathodic potentials as a function of crystal orientation using cyclic voltammetry, SEM and AFM, to determine to what extent cathodic corrosion is anisotropic in nature. Additional experiments were performed to gain insights into the effect of the presence of CO on cathodic corrosion. Carbon monoxide experiments were conducted to investigate the effect of more realistic reaction conditions on cathodic corrosion as they might be found in gold-driven CO_2-electrolyzers, although effects of the presence of CO_2 (reactant) and carbonate salts (typically present in the reaction medium) were excluded from this study. It was found that cathodic corrosion of gold is strongly anisotropic, with stepped surfaces and the {110} plane being most susceptible to dissolution, whereas the {111} and {100} planes were much more resilient to dissolution. On these more stable surfaces, nanocrystallite growth was observed instead, which we hypothesize originates from redeposition of the gold that dissolves from the more corrosive, more open and/or defective facets. Finally, the presence of carbon monoxide was found to slightly enhance the rate of surface change, as evidenced by increases in charge in cyclic voltammograms after corrosion and an earlier onset of crystallite growth on the {111} and {100} planes, which we ascribe to enhanced gold mobility due to the strong bond formed between CO and gold in alkaline media.

This chapter has been published in
Raaijman, S. J.[=]; Arulmozhi, N.[=]; Koper, M. T. M., *J. Phys. Chem. C* **2020**, *124* (52), 28539-28554.

3.1. Introduction

With the predicted strong growth of renewable energy sources[1], their intermittency will become increasingly problematic. One option for dealing with the intermittency is to electrochemically generate value-added products at times when the supply supersedes demand. The electrochemical conversion of carbon dioxide and water, or the CO_2 reduction reaction (CO2RR), would make a suitable contender for this role as it can yield a plethora of valuable products in the form of hydrocarbons, carbohydrates and (inorganic-) acids. However, the CO2RR requires a suitable catalyst to facilitate the efficient conversion of electrical work into chemical products. Fortunately, catalysts exist that are capable of reducing carbon dioxide to economically interesting products with good selectivity and efficiency: gold[2] and silver[3] are capable of forming carbon monoxide with high selectivity, indium[4] and palladium[5] are selective for the formation of formic acid and, depending on the exact conditions, copper can produce ethylene[6] or ethanol[7] with very reasonable efficiencies.

However, the applicability of a catalyst is subject to stringent performance tolerances for it to be economically viable. Two important metrics are catalyst cost and lifetime[8], since replacement of spent catalyst requires capital and leads to process downtime, reducing overall profitability. Under CO2RR relevant conditions (negative potentials, high current flows, high local pH values and large amounts of product), metals can undergo substantial morphological restructuring and possibly dissolve due to cathodic corrosion (CC).[9] Cathodic corrosion is a degradation pathway that might prove quite relevant for catalyst stability and long term performance in CO_2-electrolyzers. This phenomenon has been mainly studied on platinum electrodes[9–12], leading to the formation of nanoparticles in solution and etch pits on the metal surface, resulting in the generation of specific surface sites.[12] It has been hypothesized that these pits originate from atom clusters being expelled from the surface via the formation of a negatively charged ternary metal hydride complex.[11] The process itself has been shown to depend strongly on cation identity and concentration, and there seems to be good agreement between the onset of corrosion and the specific potential window where adsorption of a full monolayer of hydrogen becomes energetically favorable.[11]

At present, CO_2-electrolyzers focusing on HCOOH or CO production are regarded as closest to commercialization, with CO having a larger market.[13] The best catalysts for producing CO are silver and gold, both exhibiting high selectivity at low overpotentials.[2, 3, 14] However, both metals have been reported to undergo cathodic corrosion.[9]

Therefore, we explore in this work the cathodic corrosion of gold single crystal electrodes, showing evidence for a strong anisotropic effect both with regards to pitting, and for nanocrystal formation. The choice to study gold is based on the fact that the field of gold single crystal electrochemistry is mature and expansive[15–17] and experimentally more accessible.[18, 19] There already exists literature on its cathodic corrosion behavior (for polycrystalline surfaces)[9, 11, 20], showing that gold exhibits a tendency to form (nano-) crystallites on the surface.[20] An additional motivation for the work in this paper is that cathodic corrosion has been studied

predominantly under HER conditions, as opposed to CO2RR conditions.[21] Trends in macroscopic pitting and deposition phenomena as a function step type and step density were investigated on spherical single crystals (Au(sphere)), whilst cut crystals (Au(hkl)) enabled us to deconvolute electrochemical signals from Au(sphere) crystals. Finally, experiments were conducted with the addition of gaseous CO to the electrochemical cell as a means to approximate realistic CO2RR conditions.[6]

3.2. Methods

3.2.1. Electrodes, electrolytes, and electrochemical Cells

The experimental work was conducted using monocrystalline bead-type Au(111), Au(110) and Au(100) electrodes (icryst, oriented to $\leq 0.1^{\circ}$), and Au(spherical) working electrodes (WE) prepared using the flame fusion method.[22–24] Prior to each measurement, spherical single crystals were entirely regrown and flame annealed immediately prior to measuring, while cut crystals were annealed at ca. $950\ ^{\circ}C$ in a pure hydrogen flame for at least $5\ minutes$. A gold mesh (99.999%) was used as a counter electrode (CE), and a reversible hydrogen electrode (RHE) (Hydroflex, Gaskatel) was used as a reference electrode (RE). Two types of custom-made electrochemical cells were employed in this study, namely a Pyrex glass cell and a fluorinated ethylene propylene (FEP) cell. The two-compartment Pyrex glass cell was used in all CV measurements in acid media and the FEP cell was employed in cathodic corrosion measurements in alkaline media. The FEP cell consists of a single compartment with ca. $3\ cm$ of distance between the CE and the WE surface. The H_2SO_4 (96%, ultrapur, Millipore) and NaOH (30%, suprapur, Millipore) electrolyte solutions were prepared using ultra-high purity (UHP) Milli-Q water (Millipore; resistivity $\geq 18.2\ M\Omega \cdot cm$). Glassware and plasticware were cleaned by storing it in aqueous permanganate solution ($0.5\ M$ H_2SO_4 (96%, ACS reagent, Honeywell) and $1\ g \cdot L^{-1}$ $KMnO_4$ (99%, ACS reagent, Sigma Aldrich)). Prior to the experiment, permanganate residue was removed by rinsing with Milli-Q water and washing with diluted piranha solution (3:1 *v/v* mix of H_2SO_4 (96%) and H_2O_2 (30%), diluted with water) to remove manganese dioxide and permanganate residue. Next, glassware was boiled five times in Milli-Q water.

Ultra-high purity argon (Linde, 6.0) was passed through and above the electrolyte to remove any dissolved gases. Prior to establishing electrode-electrolyte contact, argon flow through the electrolyte is stopped while the argon flow above the electrolyte is maintained or initiated. After annealing the monocrystalline gold electrodes, the hot electrode is subsequently transferred to the electrochemical cell and cooled in argon atmosphere. Once cooled to room temperature, the so-called hanging meniscus configuration was used for making electrochemical contact of the Au(111), Au(110), and Au(100) electrodes. In the case of Au(spherical)[25], the electrode was carefully placed in the electrolyte so that the monocrystalline gold sphere was entirely submerged. All electrochemical experiments were conducted using a Bio-Logic SP 300 potentiostat using proprietary software. All surfaces were normalized assuming $390\ \mu C \cdot cm^{-2}$ (the value assigned to polycrystalline gold), which was deemed to best represent the imperfect nature of the cut single crystals,

and the fact that many different sites are present on spherical single crystals.[26] CVs obtained post-corrosion were normalized using the surface area calculated from the blank obtained prior to corrosion.

3.2.2. Cathodic corrosion studies

The cathodic corrosion studies were performed at Au(111), Au(110), Au(100) and Au(spherical) electrodes via application of a constant potential (E_p in the range between –1.10 V_{RHE} and –1.30 V_{RHE}) for a controlled polarization time (t_p, with $2.5 < t_p < 7.5\ minutes$) in $10\ M$ NaOH at room temperature. These conditions were chosen on account of the fact that the least cathodic potential and shortest time was close to the observable onset for surface restructuring from SEM, whereas the upper limit (most cathodic potential and longest time) showed large surface changes but could still be related to the initial faceting. Specifically, shorter times at less cathodic potentials were not tried, as the current least corrosive conditions ($2.5\ minutes$ at –1.1 V_{RHE}) exhibited only minor signs of change in SEM images. More strongly cathodic potentials ($5\ minutes$ at –1.5 V_{RHE}, not shown) were initially tested, but resulted in such drastic changes that it became impossible to correlate the initial substrate structure to the morphology observed in the SEM after corrosion. Some tests were conducted for longer times ($1.5\ hour$ at –1 V_{RHE}, Figure B.4) as well, but corrosion for such long times resulted in significant issues with surface cleanliness, being detrimental to experiment reproducibility. The electrolyte was used for either a maximum of $10\ minutes$ of corrosion time, or a total of three separate measurements (depending on which metric was reached first), after which it was discarded and the cell thoroughly rinsed, and fresh electrolyte added. All corrosion measurements were conducted using a freshly prepared electrode surface. For all corrosion experiments, Ar or CO was bubbled through the solution before *and during* the experiment. Cathodic polarization studies were conducted with the cell submerged in a water bath at room temperature with a magnetic stirrer (in the water bath) to prevent electrolyte heating.

Figure 3.1 displays a potential versus time profile that illustrates the sequence of steps (a through e) involved in the corrosion studies.

- Firstly (step a), a cyclic voltammogram (CV) is measured in $0.05\ M$ H_2SO_4 electrolyte in the potential window $0 \leq E \leq 1.65\ V_{RHE}$ at a scan rate of $\nu = 80\ mV \cdot s^{-1}$ to characterize the initial surface.

- Secondly (step b), the electrode is rinsed with Milli-Q water and flame annealed in either a hydrogen flame of ca. $950\ ℃$ for $5\ minutes$ (cut crystals) or in a butane flame until the gold surface is faintly red hot for $5\ minutes$ (spherical crystals) to remove the defects generated in step a.

- Thirdly (step c), the electrode is immersed in $10\ M$ NaOH (at controlled potential of $0\ V_{RHE}$), but not in hanging meniscus configuration in this instance. Then, the potential is stepped from $E = 0\ V_{RHE}$ to a certain (85%) iR compensated polarization potential E_p (in Figure 3.1, $E_p = -1.30\ V_{RHE}$); for a defined polarization time t_p (in Figure 3.1, $t_p = 2.5\ minutes$).

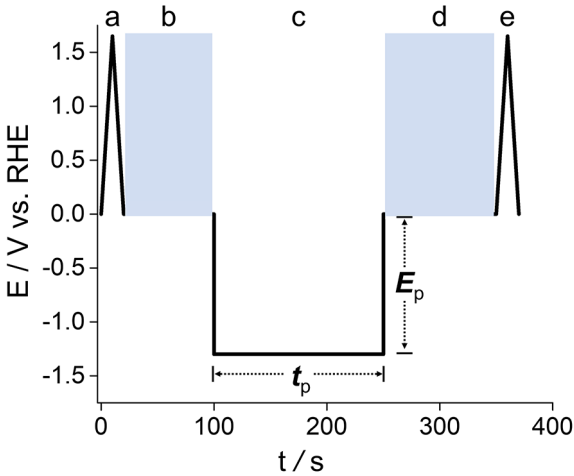

Figure 3.1: The potential program employed in the cathodic corrosion studies. Step a: cyclic voltammetry in the sulfate adsorption/desorption region and gold oxidation/reduction region in $0.05\ M$ H_2SO_4 at a scan rate of $\nu = 80\ mV \cdot s^{-1}$. Step b: Cleaning the electrode in Milli-Q water and annealing for $> 5\ minutes$. Step c: cathodic corrosion in $10\ M$ NaOH aqueous solution at a given potential E_p for a given time t_p. Step d: Cleaning the electrode with Milli-Q water. Step e: cyclic voltammetry in the sulfate adsorption/desorption region and gold oxidation/reduction region in $0.05\ M$ H_2SO_4 at a scan rate of $\nu = 80\ mV \cdot s^{-1}$.

- Thereafter (step d), the cathodically corroded crystal is rinsed with Milli-Q water for sodium hydroxide removal
- Finally (step e), the electrode surface after corrosion is characterized again via cyclic voltammetry as described in step a.

Due to the variation in the potential sensitivity of different facets with regards to adsorption of ions, cyclic voltammetry in H_2SO_4 (in the window $0 \leq E \leq 1.65\ V_{RHE}$)[15–17] can be used to characterize changes in surface structure via comparison of CV profiles obtained prior to and after cathodic treatment.

3.2.3. Microscopic analysis of cathodic corrosion

Surface roughening of the monocrystalline Au(spherical) electrodes brought about by cathodic corrosion was analyzed using Scanning Electron Microscopy (SEM, Apreo SEM, Thermo Scientific) and Atomic Force Microscopy (AFM, JPK Nanowizard 4). After the corrosion experiment, the monocrystalline Au electrode was carefully removed from the electrochemical cell and placed in a custom-made SEM sample holder. Then, the sample was rinsed under a stream of Milli-Q water to remove traces of acid from the electrode. Subsequently, the monocrystalline Au(spherical) electrode was dried in a stream of Ar(g) and placed in the SEM/AFM chamber for analysis. The SEM was operated in high vacuum condition ($< 5 \cdot 10^{-6}\ mbar$) and the images were collected at a beam setting of $10\ kV$ and $0.40\ nA$ using an Everhart-Thornley detector. The AFM measurements were conducted in contact mode, using

a gold coated tip (NANOSENSORS™ PPP-FMAuD; tip height $10 - 15\ \mu m$, tip resonance frequency: $75\ kHz$, tip force constant: $2.8\ N \cdot m^{-1}$) at a scan rate of $0.4\ Hz$. Crystals not being actively measured/used were affixed in a custom holder and stored in a plastic vial so as to minimize ambient exposure.

In order to identify the main surface facets of a Au(spherical) electrode, we compare the FCC unit cell to an SEM image of a corroded Au(spherical) electrode. Figure 3.2a shows an SEM image of an as-imaged monocrystalline Au(spherical) electrode and Figure 3.2b presents the FCC lattice structure of a Au single crystal, with the low Miller index facets depicted using different colors (i.e., {111} in red, {100} in blue, and {110} in green). In the SEM image, stereographic triangles are superimposed using grey, dashed lines. The SEM instrument was equipped with a three-axis goniometer and allowed us to orient the monocrystalline Au(spherical) electrode and to acquire SEM images that were then superimposed on the simulated single crystal. Once superimposed with reasonable accuracy ($\pm 3°$), we can identify the location of the main surface facets on the actual monocrystalline Au(spherical) electrode. One stereographic triangle in the actual and simulated single crystals is marked with black lines; it contains all basal, stepped and kinked facets. It is important to add that one FCC single crystal contains forty-eight stereographic triangles. Figure 3.2c presents a partially color-coded visualization of this triangle and shows as solid circles the locations of the facets which are the subject of our study. As explained above, the low Miller index surfaces are marked by red, blue, and green filled circles located at the vertices of the triangle; stepped surfaces are located along edges of the triangle. Kinked surfaces are located inside of the triangle.

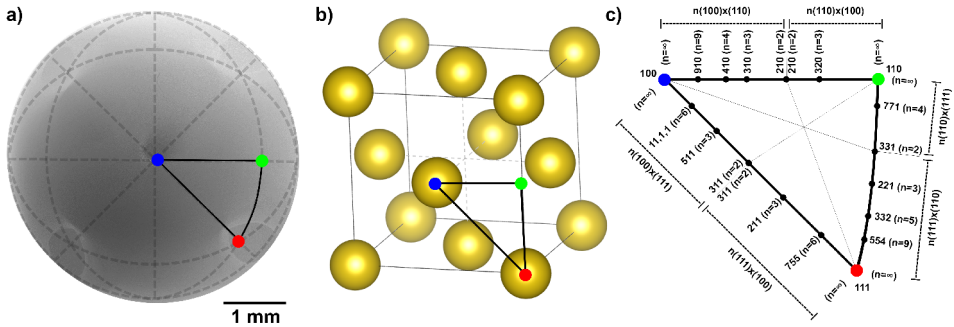

Figure 3.2: The methodology of surface facet identification on a Au(spherical) electrode. a) An SEM image of an actual (corroded) Au(spherical) electrode. b) An image of the FCC lattice that a spherical Au single crystal adopts, with the low Miller index facets depicted using different colors (i.e., (111) in red, (100) in blue, and (110) in green). One stereographic triangle in these two images is marked using a black, solid line. c) Color-coded visualization of a stereographic triangle, showing the locations of the surface structures which are the subject of our study.

Table 3.1: Different potential windows that comprise the gold oxide formation region in $0.05\ M$ H_2SO_4, adapted from work published by Štrbac *et al.*[17]

Potential window	Sites that contribute	Denotation in text
$1.35 < E < 1.40\ V_{RHE}$	111-, 100- and 110-type step-sites	"step-sites"
$1.39 < E < 1.42\ V_{RHE}$	110 terraces (infinite length, *secondary feature*) • shifts to more negative potentials and combines with primary 110 feature in the case of finite length terraces with 100-type step defects. • increases in peak current but stays in place in the case of finite length terraces with 111-type step defects.	Stepped terraces: "stepped {110}", "finite length {110} terraces"
$1.41 < E < 1.43\ V_{RHE}$	100 terraces (finite and infinite length)	"{100} terraces"
$1.43 < E < 1.46\ V_{RHE}$	110 terraces (infinite length, *primary feature*) • shifts to more negative potentials and combines with secondary feature in the case of finite length terraces with 100-type step defects. • exhibits minor shift to more positive potentials in the case of finite length terraces with 111-type step defects.	"{110} terraces"
$1.46 < E < 1.62\ V_{RHE}$	Finite length 111 terraces terminated by a 111- or 100-type step	"stepped {111}", "finite length {111} terraces"
$1.46 < E < 1.57\ V_{RHE}$	(subset) Small 111 terraces (N < 6 atoms), terminated by a 111- or 110-type step	"small {111} terraces", "small finite length {111}"
$1.57 < E < 1.62\ V_{RHE}$	(subset) Large 111 terraces (N > 6 atoms), terminated by a 111- or 110-type step	"large {111} terraces", "large finite length {111}"
$1.62 < E < 1.64\ V_{RHE}$	'Infinite' length 111 terraces	"{100} terraces"

3

3.3. Results and discussion

3.3.1. Voltammetric characterization of cathodic corrosion

Cathodic corrosion was investigated on single crystals oriented and cut to expose a specific facet, and on spherical single crystals that were not cut and thus contain a multitude of different types of facets. The changes in the cyclic voltammetry as a function of corrosion potential were investigated for the three basal planes (Au(111), Au(100) and Au(110)) as well as for a spherical single crystal (Au(sphere)), where trends observed on the former will be used to interpret behavior observed on the latter.

Cyclic voltammetry was conducted in $50\ mM$ sulfuric acid electrolyte between $0 < E < 1.65\ V_{RHE}$ at a scan rate of $80\ mV{\cdot}s^{-1}$ to facilitate comparison to literature data.[17] Under such conditions, the gold oxidation region ($1.35 < E < 1.65\ V_{RHE}$) exhibits a number of characteristic zones defined by the hydroxide/oxygen adsorption strength of a particular (set of) surface site(s). In this work, we focus on the gold oxidation region, because the effect of introducing different types of steps at differing step densities on this region has been thoroughly studied and reported. Furthermore, changes in step density result in gradual changes in the gold oxidation region. Hence, we focus on investigating the oxidation region as opposed to the double layer region. Although not discussed herein, close ups of the double layer region are provided in the supporting information (Figure B.5). The different regions, their accompanying potential window, and the way they are referred to in this work are summarized in Table 3.1.

Analysis of CV changes in the hydroxide/oxygen adsorption region will allow for the determination of global trends in the creation and destruction of specific types of facets. Rather than the direct conversion of one site to another, it is the formation of pits and/or nanocrystals that are responsible for the creation of specific sites as will be discussed later in this work. We start by discussing the cyclic voltammetry of the {111} plane, which is depicted in Figure 3.3a. For this surface, the characteristic feature of infinite {111} terrace sites at $1.63\ V_{RHE}$ is observed to decrease in current density and shift to less positive potentials after cathodic corrosion. From the assignment of the different regions of hydroxide/oxygen adsorption on gold in Table 3.1, this shift is indicative of the creation of large finite length {111} terraces with step defects. Thus, this particular change in the CV denotes the introduction of step-site defects in the 'infinite' {111} plane upon corrosion.

Simultaneously, the charge in the $1.46 < E < 1.57\ V_{RHE}$ region is found to increase as more corrosive potentials are applied, which is again evidence for {111} terraces with step defects. However, the terraces in this region are of smaller size (i.e., higher step density). As we will show below, these newly formed stepped facets likely relate to the formation of etch pits and nanocrystallites in and on the surface, respectively. Finally, the defects that were initially present in the cut Au(111) surface ($1.35 < E < 1.40\ V_{RHE}$, Table 3.1) exhibit non-monotonic behavior as a function of corrosion potential. Their quantity (i.e., the charge corresponding to their features) decreases for more moderate (i.e., less negative) corrosive

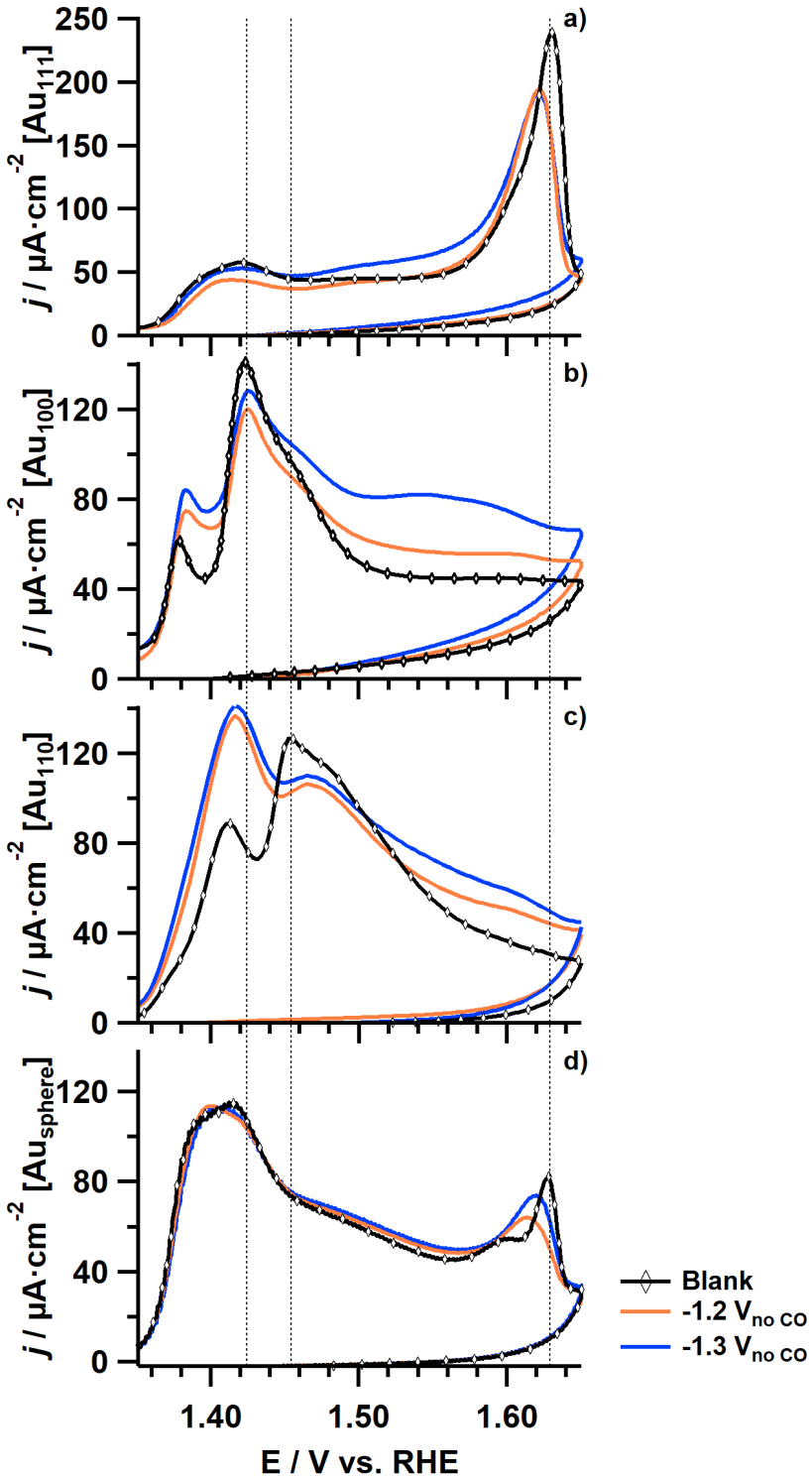

Figure 3.3: Cyclic voltammogram of a) Au(111), b) Au(100), c) Au(110) and d) Au(spherical) after 2.5 $minutes$ of corrosion in 10 M NaOH at –1.2 V_{RHE} (orange) and –1.3 V_{RHE} (blue) (85% iR corrected), compared to the blank obtained prior to corrosion (black with diamonds).

potentials, whereas this decrease in the number of these sites is less pronounced for more strongly corrosive potentials (e.g., moderate levels of CC actually result in a reduction of these type of defect sites, but this effect is less at more strongly corrosive conditions).

The voltammetry of the {100} surface is shown in Figure 3.3b. For this facet, the characteristic feature at $1.42\ V_{RHE}$ is found to initially slightly decrease in peak intensity upon corrosion. However, surfaces corroded more vigorously (i.e., having been subjected to increasingly negative potentials) exhibit less of a decrease in the number of {100} terraces than surfaces corroded under milder conditions, although the peak is still lower than for an uncorroded surface. The first observation suggests that under mild cathodic potentials (with respect to the onset of cathodic corrosion, $-0.8\ V$[20]), {100} terrace sites are being transformed and/or destroyed. The second observation can be explained by taking into account that finite length {100} terraces give rise to a broad contribution in the same region as infinite {100} terraces, the two eventually being indistinguishable from one another. Thus, although we are corroding our initially 'perfect' 100 plane, it is still possible to observe a gain in charge in the {100}-terrace-characteristic potential window if we assume that corrosion leads to the creation of finite length {100} terraces. Corrosion of the {100} terraces is further corroborated by an increase of step-site defects (feature at $1.38\ V_{RHE}$, Table 3.1) as increasingly cathodic potentials are applied. Finally, it is observed that corrosion of the {100} plane leads to a substantial increase in the number of stepped {111} terrace sites, as denoted by an increase in charge in the $1.46 < E < 1.62\ V_{RHE}$ region. Apparently, corrosion introduces specifically {111}-type step defects into the {100} surface and thereby transitions the overall surface morphology in the direction of the {111} plane.

Corrosion behavior of the most open of the basal planes, {110}, is shown in Figure 3.3c. Unlike the other two planes, this facet exhibits two characteristic features in the case of infinite terrace lengths: a weaker feature at $1.41\ V_{RHE}$ (denoted from here on as secondary), and a stronger one at $1.45\ V_{RHE}$ (which we shall refer to as primary). Under corrosive conditions, the primary feature decreases in current density. However, similar to what is observed for corrosion of the {100} plane, this decrease in peak current density is actually less when more corrosive potentials are applied. As for the secondary feature, it is found to monotonically increase with corrosion potential instead, without shifting. Finally, an increase in charge is observed for the region characteristic for finite length stepped {111} terraces. Taken together, these observations can only be explained by the transformation of the {110} plane into a surface that is rich in {111}-type sites. The fact that the primary {110} peak exhibits less of a decrease in current density as more corrosive potentials are applied, can be explained by the fact that finite-length {111} terraces contribute charge in a very broad potential range. Although the number of {110} terrace sites is expected to decrease more at stronger corrosive potentials, the contribution of charge by finite-length {111} terraces increases.

Figure 3.3d illustrates the transformation of the CV of a spherical single crystal upon cathodic corrosion. Overall, the changes in the CV of a spherical single crystal appear less pronounced than the changes for the cut single crystals. Notwithstand-

ing, the following changes are observed upon cathodic corrosion. The characteristic feature of the infinitely large {111} terrace sites at $1.63\ V_{RHE}$ is observed to shift to less positive potentials, where it is presumed to (partially) merge with the voltammetric feature characteristic of large finite width stepped {111} terraces, leading to the maximum of the latter feature shifting to more positive potentials. Furthermore, an increase in charge for smaller stepped {111} terraces is observed. This behavior mimics what is observed upon corrosion of the {111} electrode, and can be explained by the creation of step-site defects, leading to finite length stepped {111} terraces with decreasing terrace lengths as the surface corrodes further.

Finally, small changes are observed in the (stepped-) {100} terraces, and step- and kink site regions (Table 3.1). This 'twin peak' feature merges into a single peak, showing only minor changes in peak current density without clear trend. More specifically, depending on corrosion conditions (not depicted), its current density can decrease or increase marginally. Such erratic behavior is in line with the behavior observed for corrosion of Au(111) specifically, where the charge for step-site defects could increase as well as decrease, depending on experimental conditions. Although such inconsistent behavior was not observed upon corrosion of the {100} plane, it can still be reasonably explained by the {111} plane being the dominant facet on gold spherical crystals due to them adopting the equilibrium crystal shape during growth (see Figure 3.2a).[27]

Since voltammetry for stepped {111} terraces is ambiguous ({100}- and {111}-type steps cannot be clearly distinguished via hydroxide/oxygen adsorption in the CV profile), the voltammetry measurements cannot provide direct evidence for the types of steps that are formed upon corrosion of the {111} plane, it might be preferentially one step-type, or both step-types.

3.3.2. Morphological characterization of cathodic corrosion

SEM anisotropy of the basal planes

Further information regarding the facet dependency of cathodic corrosion is derived from SEM images. Because of the Au spherical single crystal adopting the FCC equilibrium crystal shape, it is possible to determine the locations of all facets, so long as one can accurately pinpoint a minimum of two facets and knows the radius of the crystal. Under the effects of corrosion, finding two identification points is straightforward as can be seen in Figures 3.4a-c. From these figures, which depict a global overview of spherical single crystal electrodes corroded for different time intervals at $-1.3\ V_{RHE}$, it can be seen that the {100} and {111} facets are easily identified.

The anisotropy in corrosion that was identified from cyclic voltammetry experiments is also observed macroscopically in the SEM images. This can be seen in the form of differences in time-dependent evolution of the different basal planes, as well as in the differences in contrast for different locations on the surface. However, the anisotropic behavior is much clearer in the images shown in Figures 3.4d-l, where close-ups of the three basal planes are presented. More specifically, Figures 3.4d-f consist of higher magnification images of the {111} plane corroded for $2.5, 5$ and $7.5\ minutes$ at $-1.3\ V_{RHE}$ in $10\ M$ NaOH, respectively, whereas Fig-

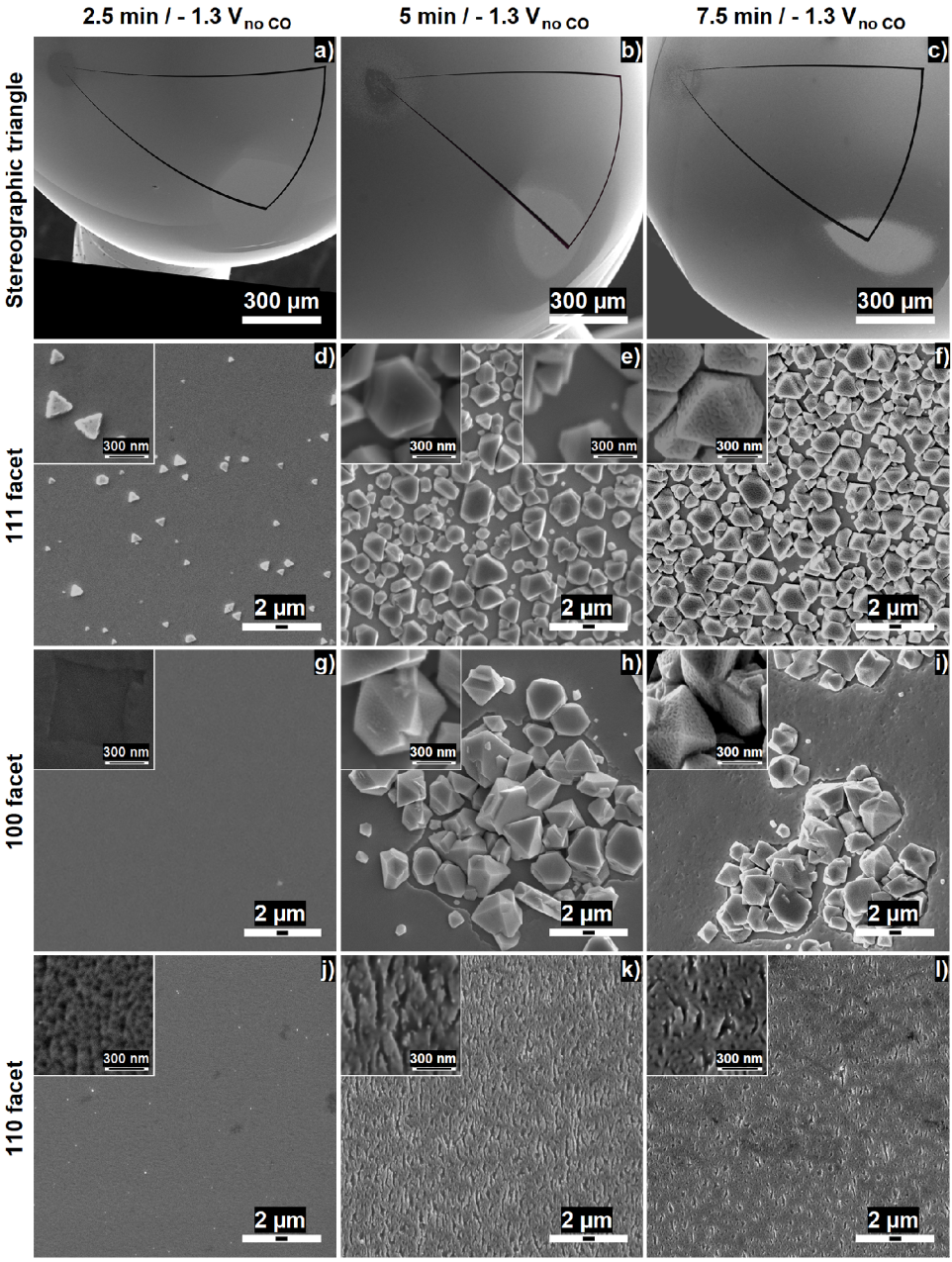

Figure 3.4: SEM images (macroscopic overview, 111 facet, 100 facet and 110 facet, respectively, going from the first to last row) of anisotropic surface corrosion in the form of pitting and nanocrystal formation as a function of time ($2.5\ min$ to $7.5\ min$, respectively, going from the left to right column) at a corrosion potential of $-1.3\ V_{RHE}$ (85% iR corrected) in $10\ M$ NaOH.

ures 3.4g-i and 3.4j-l are SEM images of the {100} and {110} faces under the same conditions.

From the expanded images, it can be seen that the morphological changes of the basal planes as a function of corrosion time differ per facet. The initially flat {111} face shows only very minor signs of pitting and etching, but does exhibit nanocrystal formation when certain corrosion potential and time thresholds are exceeded (specifically, $-1.2\ V_{RHE}$ for $\geq 7.5\ minutes$, Figures B.1a and B.1b). Of course, we realize that SEM cannot image truly nanoscopic changes on the surface. Regarding crystallite formation, uniformly distributed nanocrystals with a clear preference for triangular-prism (with the word prism denoting the top face to be parallel with and equal in shape to the base, like a column) and octahedral geometry start to form (Figures 3.4d and 3.4e), with crystallite density increasing as a function of corrosion time. Although pitting of the flat face is observed (Figure B.2a) after the onset of nanocrystal formation, these newly formed nanocrystals themselves exhibit much more prominent pitting (Figures 3.4e and 3.4f).

Compared to the {111} plane, only minor signs of surface pitting are observed for the {100} facet prior to the onset of nanocrystal formation. The earliest observed signs of pitting can be seen in Figure 3.4g (showing an uncommonly observed pit), but pits become more prevalent when nanocrystals start to grow (Figure B.2b). Again, at sufficiently cathodic conditions, nanocrystals are also observed on the 'infinite' {100} plane (specifically, $-1.3\ V_{RHE}$ for $\geq 5\ minutes$, compare Figure 3.4g to 3.4h) and these nanocrystals themselves are also susceptible to surface pitting (Figure 3.4i, inset). However, some differences exist when comparing nanocrystal formation on {100} and {111}. Firstly, the onset of nanocrystal formation is shifted to more cathodic potentials. Secondly, rather than depositing uniformly, nanocrystals on the {100} facet tend to cluster together (compare Figures 3.4e and 3.4h). Thirdly, whereas the nanocrystals that deposit on the {111} face preferentially adopt a triangular-prism geometry, the crystallites that form on the {100} face are better described as adopting shapes driven by a truncation process (where truncation refers to the (partial) cutting of the vertices of a polyhedron, resulting in the creation new faces in their stead) and/or aggregates of crystallites, with some of the smaller individual crystallites adopting an octahedral shape.

Cathodic corrosion-induced morphological changes for the {110} plane do not follow what is observed for the {111} and {100} planes. As opposed to mild surface pitting paired with nanocrystal growth under sufficiently corrosive conditions, severe surface pitting takes place without the formation of nanocrystals (see e.g., Figure 3.4l). Corrosion behavior of this facet is dominated by surface etching and pitting as can be seen in Figures 3.4j-l. The onset of pitting in the {110} face as observed in SEM images ($-1.1\ V_{RHE}$ for $\geq 5\ min$, Figures B.1c and B.1d) occurs earlier than SEM-observable morphology changes (e.g., pitting and/or nanocrystal formation) for the {111} and {100} faces, with the earliest signs of corrosion for the latter two faces requiring potentials equal to, or more negative than, $-1.2\ V_{RHE}$ at corrosion times exceeding $5\ minutes$.

The observed nanocrystal growth, where applicable, is found to depend on both corrosion time and corrosion potential. In Figures 3.4d-f, the corrosion time is varied

for the same applied potential, showing a clear increase in nanocrystal density with respect to time. The potential dependency of nanocrystal formation is evident from comparing the onset potential for nanocrystal formation on the {111} face as discussed previously (–1.2 V_{RHE} for ≥ 7.5 $minutes$, Figures B.1a and B.1b) with the onset of nanocrystal formation at an applied potential of –1.3 V_{RHE}: ≥ 2.5 $minutes$ (Figure 3.4d). This seems to suggest that nanocrystal formation depends on the buildup of a concentration gradient of dissolved gold ions, which would originate from surface etching under cathodic potentials. More cathodic potentials lead to faster dissolution, resulting in reaching supersaturation values sooner and thus an earlier onset of nanocrystal formation. However, the facets that exhibit nanocrystal deposition during corrosion experiments actually show little surface pitting prior to (and arguably after) the onset of nanocrystal formation. Rather than the flat basal planes being the origin of the gold ions, we hypothesize the gold ions to originate from the dissolution of facets with step defects as we expect them to be more corrosive.

AFM anisotropy of the basal planes

Further insight into surface dissolution and ion redeposition phenomena is derived from AFM imaging, shown for the three basal planes in Figure 3.5. Firstly, in Figures 3.5a-c, a $5x5$ μm AFM image and accompanying line profile and histogram for a corroded Au(111) surface are depicted. The AFM image agrees with SEM data (Figure 3.4e), showing nanocrystal growth with uniformly distributed nanocrystals with preferential triangular-prism geometry. From the line profile (Figure 3.5b), it becomes evident that these nanocrystals are have fairly flat tops that run parallel to the substrate on which they grow. Furthermore, the spots where nanocrystals are absent (purple-blue colored regions in Figure 3.5a) show little variation in height. Hence, the majority of the roughening occurring for this facet stems from the growth of nanocrystals, rather than from dissolution/corrosion of the surface itself. This also agrees with previously discussed SEM data, where parts of the surface that do not contain crystallites look to be 'smooth'.

An AFM image of the {100} plane, with accompanying line profile and histogram can be seen in Figures 3.5d-f, respectively. Contrary to the behavior of nanocrystal growth on the {111} plane, nanocrystals that grow on the {100} plane have the tendency to form clusters of crystallites, resulting in non-uniform surface coverage. Furthermore, the clustering results in nanocrystals that have seemingly arbitrary shapes, although smaller individual crystallites exhibit preference for an octahedral geometry, as observed from both SEM and AFM. Contrary to the smoothly terminated 'plateau-like' nanocrystals that form on the {111} face, the nanocrystals that grow on the {100} face are better described as 'mountainous'. As for corrosion of the plane underneath the nanocrystals, a fairly smooth surface can be observed; in line with what we find for the etching of Au(111).

The final facet, Au(110), is shown in Figures 3.5g-i, containing respectively an AFM image, and accompanying line profile and histogram. For this plane, no nanocrystal formation is observed upon corrosion, which is in line with what SEM data show (Figure 3.4k). However, the surface clearly exhibits pitting, with these

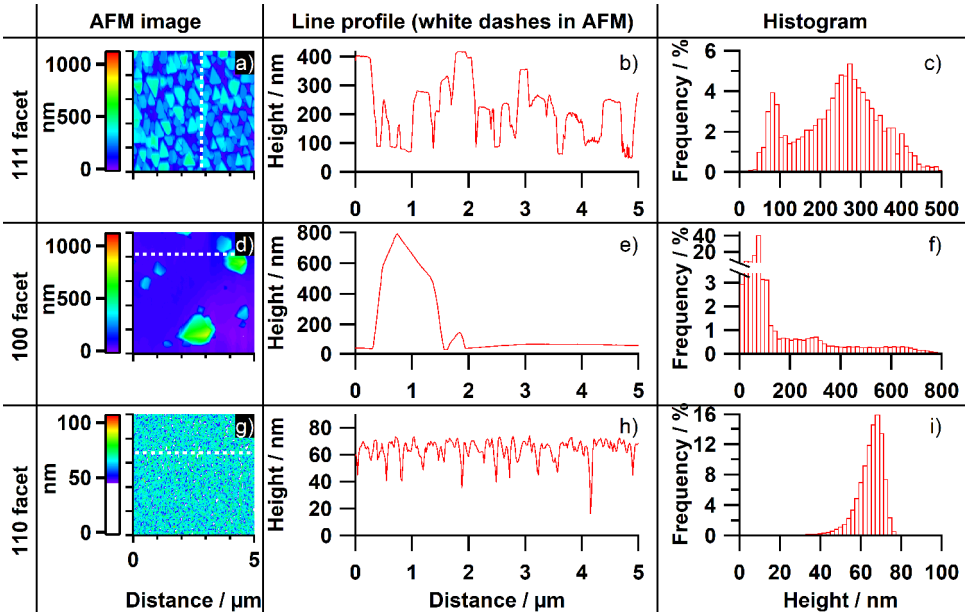

Figure 3.5: AFM images, line profiles and histograms (columns 1, 2 and 3, respectively) for the basal planes ({111}: a-c, {100}: d-f, and {110}: g-i) after cathodic corrosion at –1.3 V_{RHE} (85% iR corrected) for 5 $minutes$, in 10 M NaOH.

pits being distributed uniformly across the surface and reaching depths of several tens of nanometers.

3.3.3. Enhanced corrosion at stepped surfaces

Due to the regularity of spherical single crystals, facets with step- and kink site defects are located between the basal planes on the stereographic triangle, with the step density increasing as one moves further away from any of the three basal planes. As such, it is possible to investigate surface morphology after corrosion as a function of step type and step density by imaging different parts of the three sides of the stereographic triangle as defined by the {111}, {100} and {110} faces. The results of such an experiment are shown in Figure 3.6 (identical corrosion conditions as in Figures 3.4e, h and k), wherein we traverse along the edges of the stereographic triangle and take an image of the surface at equidistant intervals, varying step density and transitioning step types along the way.

Corrosive effect of introducing minor amounts of defects in {100} and {111} planes

The effect of incorporating a small number of step-site defects (i.e., low step density) into 'infinitely large' (unstepped) {100} and {111} terraces can be investigated by comparing Figure 3.4h ('perfect' {100}) with Figures 3.6a and 3.6o (n{100}x{110} and (n{100}x{111}) – and by comparing Figure 3.4e ('perfect' {111})

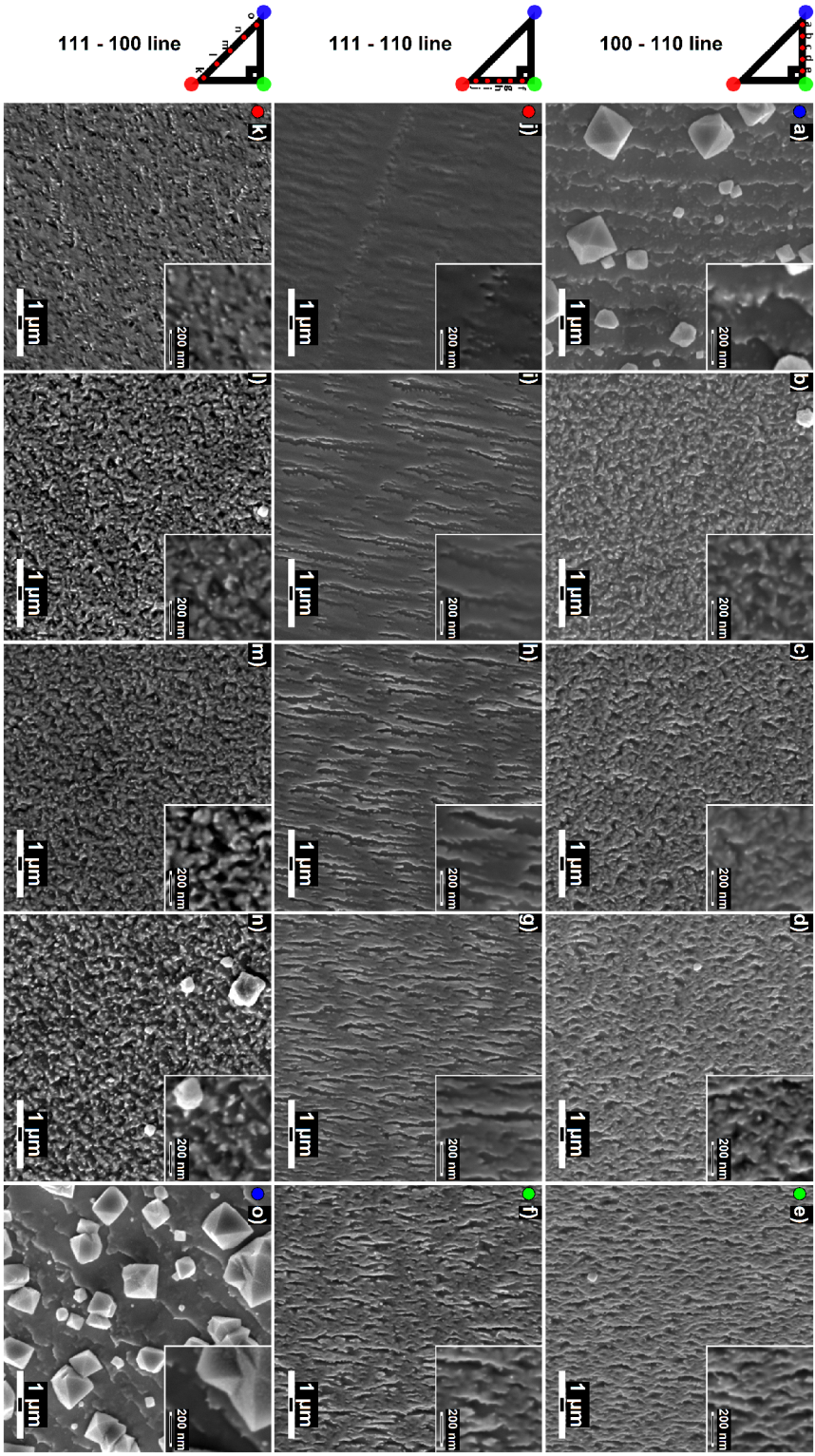

Figure 3.6: Effect of step-type and step density on macroscopic corrosion phenomena at −1.3 V_{RHE} (85% iR corrected) for 5 $minutes$, as investigated by traversing the stereographic triangle in its entirety.

with Figures 3.6j and 3.6k (n{111}x{110} and n{111}x{100}). For this comparison, we shall neglect nanocrystal growth on the infinite terraces, and focus on the areas in the SEM images that do not contain nanocrystals (e.g., in-between crystallites such as in the right inset in Figure 3.4e and/or nanocrystal-free patches, like the corners in Figure 3.4h). From these images it is found that the infinite {100} and {111} faces yield much smoother surfaces post corrosion as compared to the same surfaces with a minor density of step-site defects, which yield visually coarser surfaces upon corrosion (mind the two-fold difference in magnification between Figures 3.4 and 3.6). Since the presence of small amounts of step-site defects results in visually more roughened surfaces upon corrosion, and due to the fact that these facets with low step density are located in close spatial proximity to their unstepped counterparts, we hypothesize that dissolution of gold atoms at these stepped facets drive the concentration gradient that we think is responsible for nanocrystal formation as observed on the 'infinite' {111} and {100} faces.

Corrosive effect of varying the density of {110}-type steps in {100} and {111} planes

We start the investigation into the effect of step type and step density on corrosion behavior by looking at the effect of {110} step-site defects terminating {100} and {111} terraces (Figures 3.6a, b, c and 3.6h, i, j, respectively). From these images, it can be seen that surfaces that contain {110} step-site defects are highly susceptible towards cathodic corrosion. Interestingly, the mode of corrosion in the presence of this particular step-type seems to depend on the neighboring terrace site: {100} or {111}. Corrosion of {100} terraces next to {110}-type steps with low step density (Figure 3.6a) results in a 'staircase-like' surface with fairly straight step edges on which nanocrystallites grow. However, increasing the number of step-site defects (Figures 3.6b, c) yields a much coarser surface exhibiting uniform micro-roughening without nanocrystal growth during cathodic corrosion. Quite different morphological changes are observed when {111} terraces with {110}-type step defects undergo cathodic corrosion: firstly, both low (Figure 3.6j) and higher (Figures 3.6h, i) step densities result in a similar type of surface. Secondly, corrosion of the steps is found to yield densely packed trenches that are open-ended on one side (Figures 3.6h, i) with the number of trenches per unit area diminishing as step density is reduced (Figure 3.6j). Overall, the surface morphology after corrosion becomes 'smoother' for the facets with fewer step-site defects, leading to the observation that the {111} terraces by themselves are less corrosive than when terminated by {110}-type step defects. This observed difference between corrosion of {111} facets and {100} facets in the presence of {110}-type steps may, in part, originate from redeposition phenomena. Specifically, the onset of nanocrystal formation on the {100} plane is observed to initiate at the edges of this face, where the terraces with low density step defects are located (Figures B.3a and B.3b) before they start to form aggregrates on the defect-free facet, as opposed to crystallite formation on the {111} plane (see e.g., Figures B.1a and B.1b), where nanocrystals are only observed on the defect-free face.

Corrosive effect of varying the density of {100}- and {111}-type steps in {110} plane

The presence of {100}- and {111}-types of step defects in {110} terraces is found to have much less of an enhancing effect on corrosion susceptibility than the presence of {110}-type step defects in {111} or {100} terraces. Specifically, in the case of {100}-type step defects in {110} terraces with low (Figure 3.6e) and higher (Figures 3.6c, d) step density, it is found that step- and terrace-sites cannot be distinguished in the SEM images and that the surface morphology remains virtually identical as step density increases. This, combined with the strong resemblance of the morphology of these surfaces with the morphology of corroded {110} terraces without step-site defects (Figure 3.4k), indicates that post-corrosion morphology is dominated by corrosion of the {110} terrace sites, and indifferent to the presence of {100} step-sites.

Corrosion of {110} terraces in the presence of {111}-type steps of low (Figure 3.6f) and higher (figures 6g, h) density exhibits behavior comparable to the presence of {100}-type steps; yielding in a surface containing many pits that are a few hundred nanometers in size. However, unlike {100} step-sites, increasing the density of {111}-type steps (going from Figure 3.6f to h) does lead to morphological changes. Specifically, the pits become more elongated to yield trenches, which in turn become seemingly open ended on one side as the step density is further increased. Rather than stating that these morphological changes originate from the presence of increased amounts of {111}-type steps, it is more accurate to state that corrosion of the {110} terraces transitions into corrosion of {110}-type step sites. This reasoning can be substantiated by comparing the facets we just discussed to the facets located closer to the {111} basal plane along the same stereographic line (Figures 3.6i and 3.6j). These latter images are of corroded {111} terraces with differing amounts of {110}-type step defects, and exhibit the same types of trenches as the corroded {110} terraces with {111}-type step defects. As the trenches decrease as we get closer to the {111} plane, the {110}-type steps yield the trench-like corrosion feature as opposed to corrosion of {111}-type steps. Therefore, the changes in surface morphology upon increasing the step density of {111}-type defects in {110} terraces are better described by stating that the corrosion behavior of {110} terraces evolves to resemble the corrosion of {110}-type steps as terrace width is decreased.

Corrosive effect of varying the density of {100}-type steps in {111} plane and {111}-type steps in {100} plane

Corrosion of {111} terraces in the presence of low (Figure 3.6k) and higher (Figures 3.6l, m) density of {100}-type steps yields a morphology that is quite different from corrosion in the presence of {110}-type steps. Rather than a relatively smooth surface with trenches, a uniformly roughened surface is obtained instead. Furthermore, the surface morphology does not change much when the density of step-site defects is increased (going from 3.6k to 3.6m). As such, it is concluded that morphology is dictated by corrosion of the ({111}) terrace sites rather than by corrosion of the {100} step-sites.

The final effect that can be studied from these images is the corrosion behavior of {100} terraces with lower (Figure 3.6o) or higher (Figures 3.6m, n) densities of {111}-type step defects. Corrosion of terraces with high amounts of step defects yield a morphology that resembles corrosion of {111} terraces, whereas lowering the step-site density further (Figure 3.6o) results once more into a 'staircase-like' morphology with fairly straight edges and crystallite formation, as was also observed in the case of corrosion in the presence of low step density {110}-type step defects. Hence, the morphology is dominated by corrosion of step-site defects, rather than of the {100} terraces.

Summarizing, corrosion resistivity of the three basal planes and their stepped counterparts is found to increase in the following order:

{110} terraces ≈ stepped {110} terraces < terraces with {110} steps < other stepped terraces < {111} terraces < {100} terraces

where:

- The presence of any type of {110} site leads to the formation of preferentially oriented trenches, which is more pronounced in the case of steps.
- Stepped {111} terraces exhibit homogenous micro-scale roughening in the presence of {100} steps, compared to trench formation in the presence of {110} steps.
- Stepped {100} terraces exhibit uniform roughening at higher step densities, and 'staircase-like' morphology with nanocrystal growth at lower step densities.
- 'Infinite' {111} and {100} basal planes exhibit the highest corrosion resistance, with the latter showing a later onset for nanocrystal formation and surface pitting.

3.3.4. On the location, shapes, and origin of nanocrystallites

In the preceding sections, we have shown that facet-specific morphological changes occur during cathodic corrosion of gold. Specifically, the {110} face and facets with higher Miller indices exhibit cathodically induced surface dissolution resulting in pitting, whereas the {111} and {100} faces mostly show nanocrystallite growth which, we hypothesize, originates from the gold that dissolves at the more corrosive facets. Dissolution from the only other possible source of gold, the counter electrode, was excluded based on the following. Firstly, nanoparticle formation on gold during cathodic corrosion has been reported in the literature before, in a work in which a titanium counter electrode (CE) was used, with crystallite shapes matching what is observed in this work.[20] Secondly, similar crystallite growth was observed over the entire crystal, both for the faces pointing towards the counter electrode and for the faces on the opposite side of the crystal - meaning there is no effect of the placement of the counter electrode on crystallite formation. The non-uniform

concentration gradient that would result from dissolution of the counter electrode would most likely not allow for such observed symmetry. Thirdly, although it is known that gold dissolution takes place at anodic potentials, the majority of the dissolution actually occurs following reduction of the oxide rather than during the anodic period of a CV.[28, 29] As a DC signal was applied during measurements, no such cycling occurred on the CE. Furthermore, gold is known to exhibit a decrease in dissolution rate (passivation) as increasingly positive potentials are applied (with commonly observed CE potentials in the +3 V_{RHE} range in this work).[28] Finally, cathodic corrosion for much longer times (1.5 $hours$) at a slightly lower cathodic potential (–1 V_{RHE}) in the presence of CO did not yield any NP formation even though the CE for this experiment was still at ca. +2.5 V_{RHE} (Figure B.4).

Surface dissolution is commonly observed during cathodic conditions for various noble metal surfaces[9, 11, 20, 21, 30], and is hypothesized to occur via the formation of a negatively charged ternary metal hydride complex.[9, 11, 31, 32] Interestingly, for platinum[33] and rhodium[20], solution phase nanoparticles are observed at sufficiently high electrolyte conditions and sufficiently negative potentials, where agglomeration and deposition of these solution-phase formed particles back onto the substrate is hypothesized to be the source of the nanoparticles that are (sometimes) observed on these surfaces after cathodic corrosion.[9] However, in this work no indications for the formation of such solution phase particles (in the form of a color change of the electrolyte, or the formation of a 'particle cloud' during corrosion, or the formation of a precipitate after cathodic corrosion) have been observed, even at applied potentials as negative as –1.3 V_{RHE}. Yet, nanocrystallite growth is observed at such potentials. Furthermore, the crystallites are only observed to grow on facets of specific crytallographic orientations ({111} and {100}), with the underlying surface seemingly having a 'templating effect', influencing the shapes of the crystallites that grow thereon.

It has been reported that for shape manipulation of gold nanoparticles there exist two distinct mechanisms.[34] Firstly, one can control the rate at which a dissolved precursor-ion is converted to the solid state, denoted as kinetic control. The second mechanism is based on selective surface passivation, whereby the growth of a particular facet is retarded due to it being blocked by some adsorbing species. In case of kinetic control, thermodynamics-driven shapes are obtained in the limiting case of infinitely slow growth rates, with thermodynamically less stable particles being formed as growth rate is increased. In case of selective surface passivation, the eventual particle shape will be such that its surface is entirely comprised of the facet that is being blocked.

If the crystallites that we observe herein were directed by selective surface passivation, their shapes should be similar/equal everywhere as the electrolyte contains the same possible adsorbates everywhere. Furthermore, under such circumstances, no substrate directing effects would be expected, yet are observed in this work. Hence, the shapes of the formed nanocrystallites must be under kinetic control instead. This would be plausible if our hypothesis of the origin of the solution-phase gold ions is correct (i.e., stemming from dissolution of more corrosive facets), as then the concentration of gold ions is location specific due to lattice periodicity.

In the case of kinetic control, particles with truncated bitetrahedral (e.g., triangular prism-like) and octahedral shape are expected for slower growth rates, whereas more complex shapes (i.e., containing more edges, having lower symmetry) are expected in the case of faster growth. Slow growth rate particle shapes agree well with the shapes observed in this work for the nanocrystallites that grow on the {111} face, validating our assumption that growth is under kinetic control. However, the shapes of the nanocrystallites that form on the {100} face exhibit a plethora of differing geometries which is difficult to reconcile with a specific expected particle shape (although some of the smaller, individual ones adopt an octahedral geometry). We think the following discussion can reasonably explain such irregular shapes as observed for the {100} face.

The onset for crystallite growth is different on the {111} and {100} faces, with the {111} face exhibiting nanocrystal formation much prior to crystallite growth occurring on the {100} face. As no typical signs of solution phase nanoparticle formation were observed, we hypothesize that seed formation takes place on the substrate, with seeds forming (and growing) earlier on the {111} facet than on the {100} facet. If a seed that forms on the substrate adopts the underlying substrate structure, then seeds that form and grow on the {111} face are thermodynamically more favorable than seeds that grow on the {100} face in the case of gold. We hypothesize this would result in a lower barrier for nucleation of seeds on {111}, thus requiring a lower local ion concentration (i.e., driving force), resulting in (and observed as) an earlier onset for nanocrystallite formation on the {111} face. Crystallite shapes in this instance match the expected shapes for particles forming under kinetic control with a slow growth rate. Considering that seeds forming on the {100} face would by the same reasoning adopt the {100} geometry, their nucleation and growth is thermodynamically less favorable, resulting in a higher barrier of seed formation and slower crystallite growth. In turn, this would decrease the rate at which gold ions are consumed, allowing for a larger local concentration gradient to build up which translates into a higher driving force, leading to more unfavorable particle shapes becoming thermodynamically viable. As a certain threshold concentration is reached, nucleation and growth barriers are overcome and growth rates increase rapidly, resulting in the formation of irregular nanocrystallites with non-equilibrium shapes.

As for why only nanocrystallite formation and growth is observed on the {111} and {100} faces, a simple stability argument can be used. Under cathodic conditions, it is evident that the {110} face and facets with higher Miller indices are unstable, as they are oberved to strongly corrode cathodically. Only the {111} and {100} faces are (relatively) stable, and hence only seeds of these orientations are thermodynamically viable. Thus, nanocrystallites only form on these faces, and not on any others. Hence, for the nanocrystallites in this work to form where they do (and do not), two conditions have to be met. Firstly, seed nucleation must take place only on the substrate (where its orientation is influenced by the substrate) and not in solution. Secondly, a sufficiently high concentration of solution-phase gold ions must be present and/or be allowed to develop.

3.3.5. Effect of carbon monoxide on cathodic corrosion of Au

Voltammetric characterization of CO effect on cathodic corrosion

To investigate the effect that CO_2 reduction taking place on gold would have on cathodic corrosion in a controlled setting, the following experiment was conducted. Cathodic corrosion was carried out $10\ M$ NaOH, to facilitate comparison with prior cathodic corrosion literature as well as to mimic the high local alkalinity expected for CO_2-electrolyzers operated at high current densities.[35] As gold is a good catalyst with high faradaic efficiency and activity for the CO2RR to CO, the concentration of CO near the surface will be high. Hence, CO2RR conditions were approximated by addition of gaseous CO to the cell during corrosion experiments. With these settings, local pH effects on cathodic corrosion can be excluded as pH changes can be neglected due to the high starting pH. Additionally, the continuous purging of the electrolyte with CO (which is not further reduced on gold) yields a constant concentration of carbon monoxide near the surface that is independent of current density. Although fixing the electrolyte pH allows one to determine solely the effect of the presence of CO on catalyst stability at an interface that is mostly independent on current density, this comes at the cost of neglecting any (possible) additional effects of the presence of CO_2 (aq) and bicarbonate/carbonate in the electrolyte. Therefore, any observed changes in the presence of carbon monoxide reflect only part of the stability differences of gold under CO2RR conditions compared to cathodic corrosion during HER. Although strategies involving strongly alkaline electrolytes have been reported as a means of boosting the overall performance of CO_2-to-CO electrocatalytic systems[36], the electrolyte conditions ($10\ M$ NaOH) are not representative of the most commonly reported conditions in established literature (generally in the $0.1 - 0.5\ M$ $KHCO_3$ range)[37]. It does, however, provide for an interface where pH changes due to changes in current can be neglected (whereas the interfacial pH of bicarbonate electrolytes is known to deviate significantly as a function of current density).[38] Furthermore, it significantly enhances the rate at which a surface undergoes changes under cathodic potentials, which allows for shorter experiments.

It is important to note that cathodic corrosion in general is more prevalent at higher cation concentrations, although it has been shown to also occur at lower cation concentrations, albeit at a slower rate.[11, 33] As for gold specifically, there are currently no corrosion data for less concentrated electrolytes ($\leq 1\ M$), but the data available in literature indicates that gold and platinum exhibit comparable behavior, in the sense that corrosion is less pronounced at lower cation concentrations (but still takes place), and that similar types of sites are created irrespective of cation concentration, though the final state of the surface will likely still be different.[11]

In Figures 3.7a-d, CVs obtained after corrosion experiments in the absence (solid lines) and presence (dashed lines) of CO are depicted for the {111}, {100} and {110} basal planes and a spherical single crystalline surfaces, respectively. A close up of the double layer region for this figure, which encompasses all CVs discussed in this work, can be found in the supporting information (Figure B.5). It is found that all surfaces exhibit the same trend when comparing CVs of crystals corroded

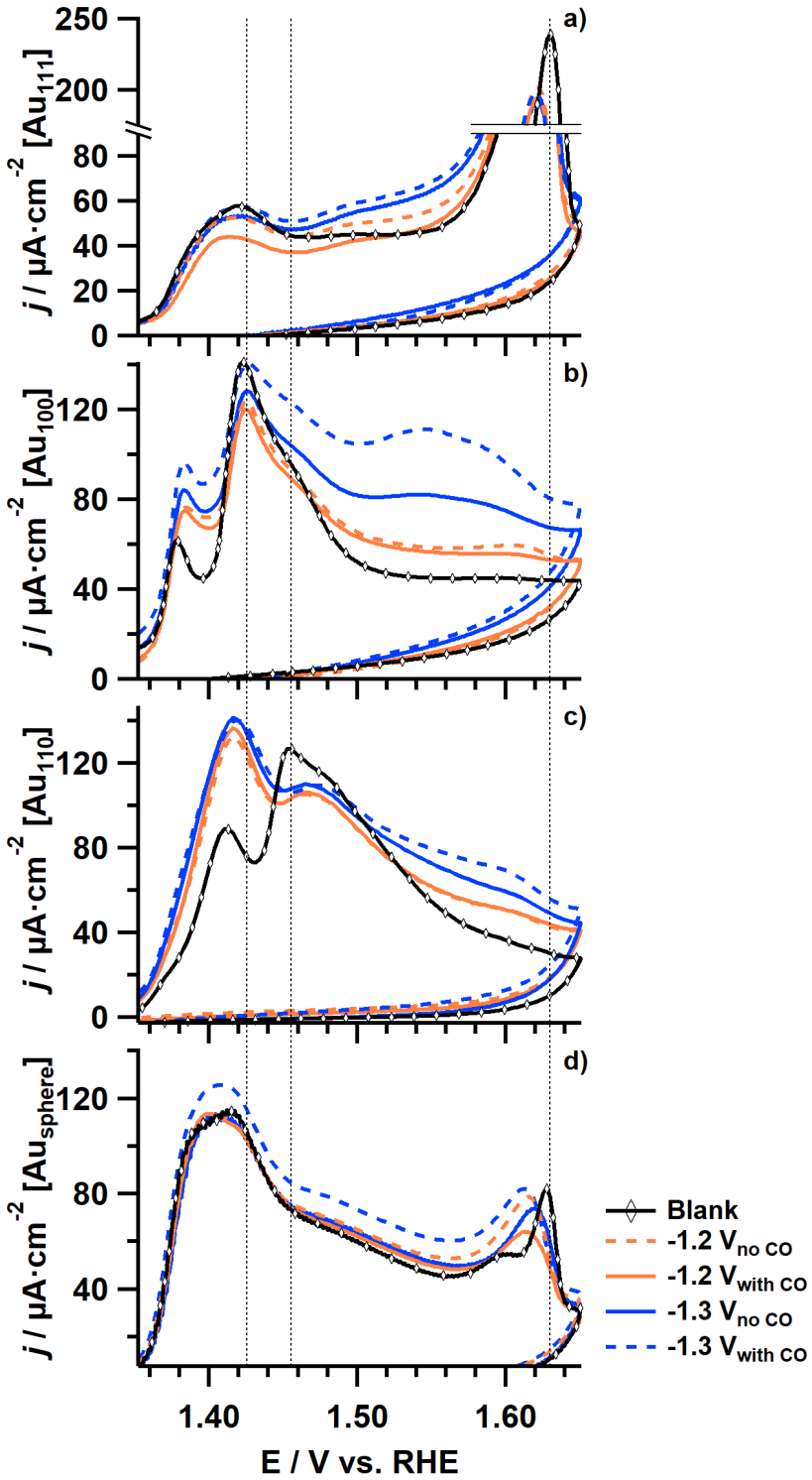

Figure 3.7: CVs of gold single crystals corroded in $10\ M$ NaOH for $2.5\ minutes$ in the absence (solid lines) and presence (dashed lines) of CO at $-1.2\ V_{RHE}$ (orange) and $-1.3\ V_{RHE}$ (blue) (85% iR corrected) for a) Au(111), b) Au(100), c) Au(110) and d) Au(spherical) electrodes, compared with their respective CVs prior to corrosion (black with diamond).

in the absence of CO with CVs of crystals corroded in the presence of CO, and therefore only one facet will be discussed. As the CO effect is most pronounced for the {100} face (Figure 3.7b), that surface will be discussed. When comparing the solid orange line (CV after $2.5\ min$ of corrosion at $-1.2\ V_{RHE}$ without CO) with the dashed orange line (CV after identical corrosion conditions but with CO present), it can be seen that there is a slight excess in charge when CO was present during corrosion. The same is observed when comparing the solid blue curve (CV after $2.5\ min$ corrosion at $-1.3\ V_{RHE}$ without CO) with the dashed blue line (corroded with CO present), albeit more pronounced. However, although the charge under the curves is found to increase (indicative of an increase in active sites), the overall shape remains mostly the same except for some small changes in the stepped-{111} region. Hence it is concluded that the presence of CO enhances the rate of corrosion but the types of sites that are generated during the corrosion process are very similar, with perhaps a small increase in stepped {111} sites. This conclusion is generalizable to the three basal planes as they show the same trend when CO is added as discussed for the {100} face. Spherical crystal surfaces are also found to be similarly influenced by the presence of CO, but from these measurements it is not possible to ascertain whether this is applicable to all the facets that constitute the overall surface, or whether all of the changes are solely due to enhanced corrosion of the {111}, {100} and {110} terrace sites that are present.

A more quantitative proof for the effect of CO on cathodic corrosion is shown in Figure B.6, wherein the roughness factors (RFs) for the crystals corroded under different conditions are depicted. Depending on the exact conditions and initial surface structure, corrosion in the presence of carbon monoxide yields an increase of 2-20% in surface area post-corrosion, compared to the surface area after corrosion in the absence of CO. However, because the effect can be seen to be highly dependent on the initial surface structure and applied potential, we believe it is more appropriate describe the effect in qualitative terms rather than quantitative terms, and hence refer to it as a 'mild enhancement'.

SEM characterization of CO effect on cathodic corrosion

In Figure 3.8, an image is depicted that is mostly identical to Figure 3.4, with the only change being that corrosion was conducted in the presence of CO as opposed to Ar. The same observations as made for surfaces corroded in the *absence of CO* are applicable here. When comparing these two datasets, it is important to be aware of the fact that each SEM image only depicts a selected spot on the surface that we deemed to best portray the particular features of that face. Most notably, on this length scale, there is some variability in nanocrystal density. Hence these particular sets of images (Figures 3.4 and 3.8) do not allow for fair comparison of the average number of nanocrystals per unit area, for which the reader is, instead, referred to Figure 3.9.

Clear evidence for the slight enhancement of surface dissolution in the presence of CO is provided in the SEM images depicted in Figure 3.9. From the micrographs depicted in 3.9a and 3.9b, it can be seen that no nanocrystal growth is observed on {111} for $t_p \leq 5\ minutes$ at a corrosion potential of $-1.2\ V_{RHE}$ when CO is absent. However, nanocrystals are found to be present after $5\ minutes$ when CO

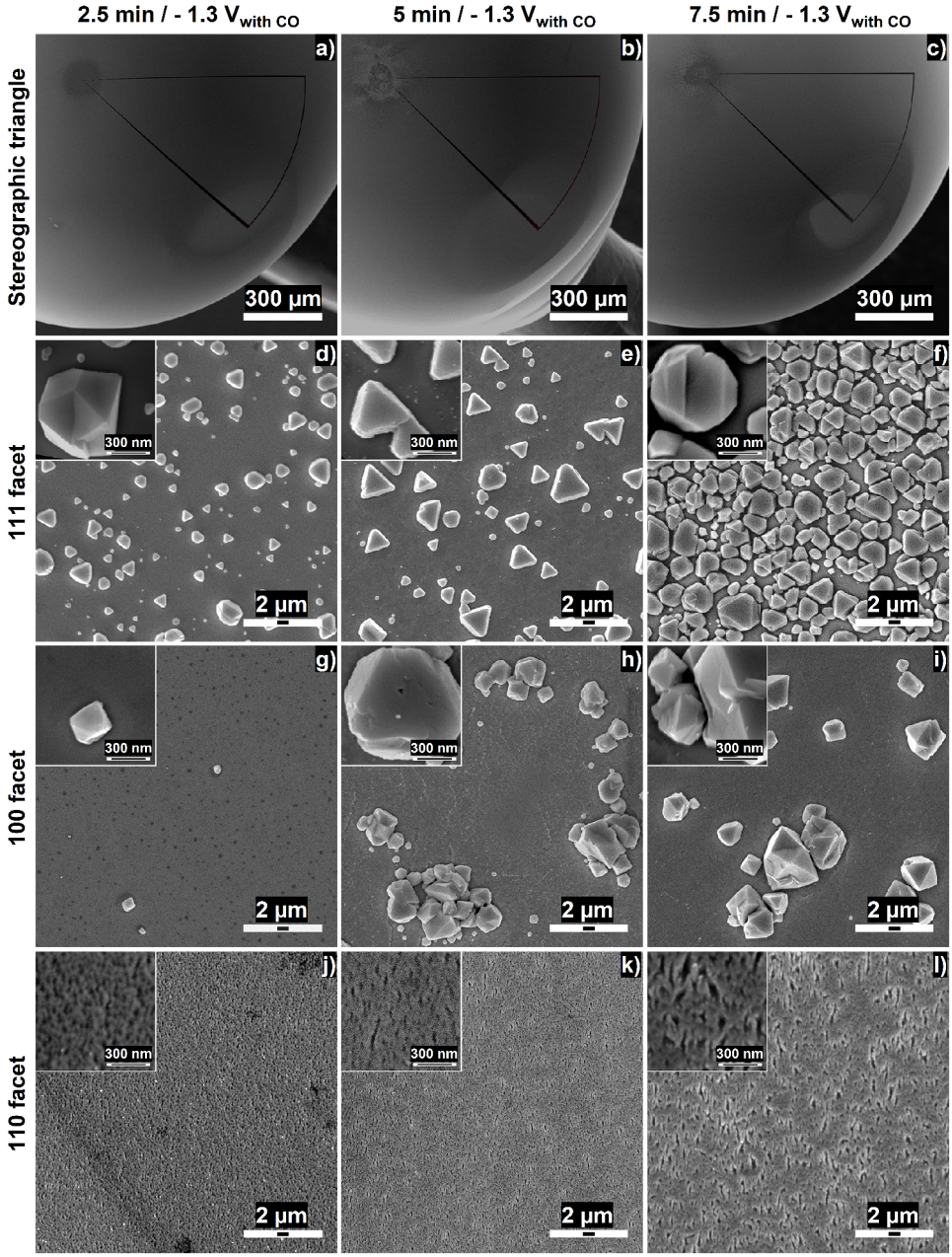

Figure 3.8: SEM images (macroscopic overview, 111 facet, 100 facet and 110 facet, respectively, going from the first to last row) of anisotropic surface corrosion in the form of pitting and nanocrystal formation as a function of time ($2.5\ min$ to $7.5\ min$, respectively, going from the left to right column) at a corrosion potential of $-1.3\ V_{RHE}$ (85% iR corrected) in $10\ M$ NaOH with CO present.

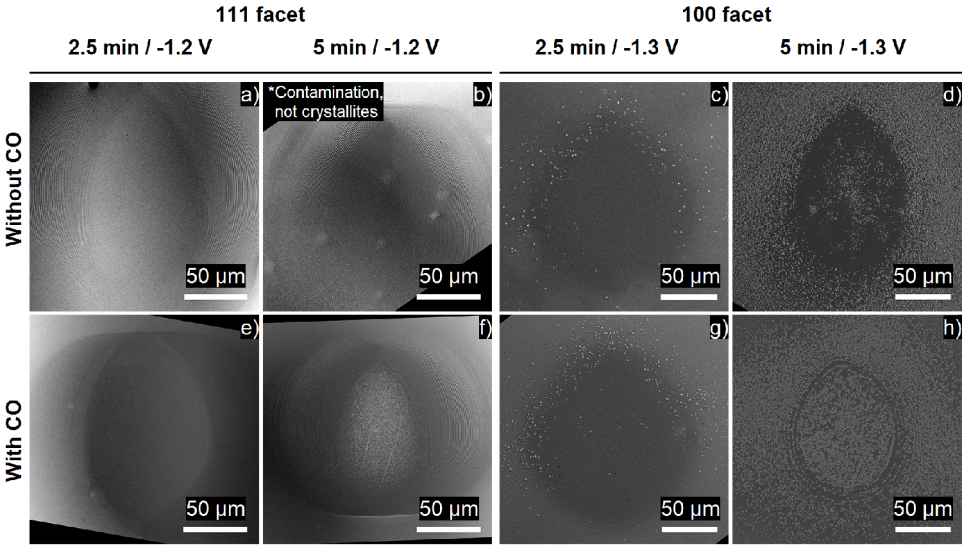

Figure 3.9: Corrosion-time dependent nanocrystal growth during corrosion in the absence (a-d) and presence (e-h) of CO at a potential of –1.2 V_{RHE} (85% iR corrected) for the 111 facet (a,b and e, f) and –1.3 V_{RHE} (85% iR corrected) for the 100 facet (c,d and g,h).

is present during corrosion under otherwise identical conditions (Figures 3.9e,f). Although the gold ions that redeposit in the form of nanocrystals likely originate from elsewhere on the surface, the fact that crystallite growth is observed sooner does indicate enhanced dissolution in the presence of CO. Similar behavior is observed for nanocrystal growth on the {100} facet (compare Figures 3.9c,d with 3.9g, h) for more negative applied corrosion potentials (–1.3 V_{RHE}). However, in both instances, this trend is only observed for crystallite formation near the observed onset of growth, and does not apply to longer timeframes and/or more corrosive potentials.

AFM characterization of CO effect on cathodic corrosion

AFM images obtained upon corrosion in the presence of carbon monoxide are depicted in Figure 3.10. Observations pertaining to surface roughening and crystallite shapes are in line with those previously discussed for corrosion in the absence of CO. However, the influence of CO on the growth of nanocrystals on the {111} and {100} faces can clearly be seen from the histograms. In both instances (Figure 3.10c for {111} and Figure 3.10f for {100}), the histograms show that in the absence of CO average height is lower. Thus, the presence of CO yields deposits with similar shapes but overall taller crystallites. The face that does not exhibit crystallite growth (i.e., Au(110)) does not display a strong CO effect, exhibiting only small changes in the histogram on the order of ca. $10\ nm$.

We attribute the slight enhancement of surface corrosion in the presence of CO to the interaction of carbon monoxide with the gold atoms at the surface. As CO is known to bind quite strongly to gold atoms in alkaline media[39, 40], the

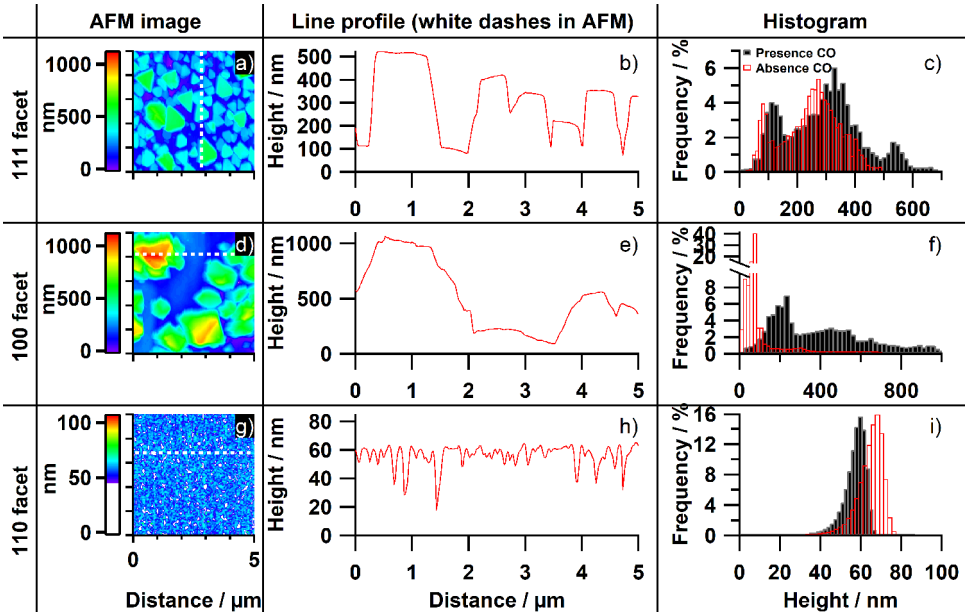

Figure 3.10: AFM images, line profiles and histograms (column 1, 2 and 3, respectively) for the basal planes ({111}: a-c, {100}: d-f, and {110}: g-i) after cathodic corrosion at –1.3 V_{RHE} (85% iR corrected) for $5\ minutes$, in $10\ M$ NaOH with CO present.

surface mobility of those gold atoms is expected to increase (as binding an adsorbate decreases the binding strength a gold atom has with its neighboring gold atoms).[41, 42] Such effects can negatively influence catalyst stability under cathodic conditions in an industrial setting, as many possible adsorbates will reasonably be present.

3.4. Discussion and conclusions

In this work, cathodic corrosion has been studied on gold surfaces with well-defined surface structures so as to determine the types of surface sites that may be preferentially created when specific types of facets corrode. Specifically, cyclic voltammetry was utilized to study changes in the hydroxide/oxygen adsorption region in $0.05\ M$ H_2SO_4, after corrosion. Voltammetric changes of cut single crystals of the three basal planes; {111}, {100} and {110}, and those of (uncut) spherical single crystalline surfaces, were investigated and compared. The inclusion of spherical single crystal electrodes enabled us to study further, using SEM, not only the macroscopic morphological changes of the three basal planes with corrosion potential (E_p) and corrosion time (t_p), but also the effect of the specific type and density of step defects present in a specific terrace. Additional information regarding the nano/microscale surface morphology for the three basal planes was obtained from AFM imaging. Finally, all parameters were investigated for surfaces corroded in the absence and in the presence of carbon monoxide during corrosion. The inclusion of

CO as a parameter serves as a controlled test environment that is meant to approximate, in part, the local environment of a gold surface if it were to be utilized in a CO_2 -electrolyzer. This parameter serves as an indication whether cathodic corrosion is influenced by the reaction that is occurring at the interface (although the absence of CO_2 (g) and bicarbonate/carbonate salts are artificially imposed simplifications of the system).

From cyclic voltammetry, SEM, and AFM, it was found that cathodic corrosion is anisotropic, i.e., dependent on the specific crystallographic orientation of the substrate. CV data showed that corrosion of {100} facets results in the preferential creation of stepped-{111} surface sites, and the same holds true for corrosion of the {110} plane. Due to the fact that the {111} face itself also undergoes corrosion (resulting also in a surface that, voltammetrically, resembles a stepped-{111} surface), it is concluded that, under cathodic conditions, the surface changes in such a way that more stepped-{111} sites are created at the cost of other types of surface sites. The presence of CO during corrosion seems to accelerate corrosion slightly (as derived from CV charges), but the overall shape of the hydroxide/oxygen adsorption region remained very similar, except for possibly a slight increase in the fraction of stepped-{111}. Therefore, the presence of carbon monoxide enhances the rate of corrosion only mildly and does not lead to a substantial shift in the types of sites that are created.

Further proof for anisotropic corrosion is obtained from both SEM and AFM, by looking specifically at corrosion of the three basal planes. On two of these faces ({111} and {100}), nanocrystal growth is observed after certain threshold potentials and corrosion times are exceeded, whereas crystallite formation is absent entirely for the {110} facet. Additionally, nanocrystal shapes, spatial distribution, and onset of formation are also facet dependent. Specifically, nanocrystals shaped like triangular-prisms that are distributed uniformly on the surface form on the {111} face, whereas smaller individual octahedra and clusters of irregularly shaped crystallites form on the {100} face. Interestingly, nanocrystal formation on the {100} facet requires longer corrosion times and more corrosive potentials than growth on the {111} face. Also, near the onset, crystallite formation on Au(100) is actually observed to start at the edges of this facet on a spherical single crystal, where {100} facets with low step density are located. This is in contrast with nanocrystal formation on the {111} face, which only takes place on the step-defect free facet. Further information regarding the crystallites that form on the two basal planes was obtained via AFM, which shows that the nanocrystals that grow on the {111} face are terminated with a flat top that runs parallel to the base, much like a plateau, as opposed to the agglomerates that form on the {100} face which are better described as irregular mountains. Furthermore, AFM has shown that nanocrystallites that form under corrosion in the presence of CO are higher than crystallites that form in the absence of CO. In a similar direction, SEM data shows that the onset of crystallite growth is shifted to shorter corrosion times or yields higher nanocrystallite densities for the same corrosion times (limited to specifically timeframes near the onset of crystallite formation) when CO is present during cathodic corrosion.

Contrary to the nanocrystal formation observed on Au(111) and Au(100), the

{110} face exhibits strong pitting and no crystallite growth under corrosive conditions. Furthermore, the formation of pits is observed to occur at less strongly corrosive applied potentials and shorter corrosion times from SEM than the conditions required for nanocrystal formation (and surface pitting) on the other two basal planes.

In conclusion, cathodic corrosion of gold can be divided into two corrosion modes: dissolution and pitting, and redeposition. As our experiments show nanocrystallite formation to be a function of corrosion time, we conclude that there must exist a concentration gradient that develops over time, resulting into electrocrystallization at specific surface sites when certain critical values are reached. Rather than gold ions dissolving and redepositing on the same face, SEM imaging shows that facets containing {110} sites (both terraces and steps), and facets with increasing amounts of step-site defects, exhibit more roughening upon corrosion than the {111} and {100} terraces with fewer to no step-site defects (which are the facets where nanocrystal growth occurs). Hence, we conclude that electro-dissolution of more corrosive facets (those containing {110}-type sites and/or having high defect density) results in the build-up of a concentration gradient of gold ions near the surface, which subsequently recrystallize on the faces that are less corrosive (i.e., more stable; defect-free {111} and {100} terraces with little to no defects). The fact that the presence of CO enhances corrosion rates leads to this concentration gradient developing faster, and hence can explain a shift in the onset for crystallite formation. Presumably, the effect of CO is related to the chemisorption of CO on gold in alkaline media[39, 40], thereby slightly weakening the Au-Au bond and enhancing surface atom diffusion.[41, 42]

Anisotropic cathodic corrosion has also been observed for Pt electrodes in alkaline media.[12, 43] However, cathodic corrosion of platinum leads to substantially different surface transformations. For platinum, the {111} facet is the most prone to cathodic corrosion, and the {110} the least, and leads to the preferential formation of {100} surface sites, both steps and terraces. Only etch pits are observed on Pt, without evidence for redeposition, with etch pit shapes reflecting the atomic order of the surface. The observed structures on platinum suggest that the etching process is (surface-) diffusion limited. The fact that gold exhibits very different behavior may suggest that the intermediate of cathodic corrosion (presumably a ternary metal hydride) has a different structure and/or stability in the case of gold, and that the role of mass transport in the generation of the surface roughness is different.

Finally, our experiments have shown that cathodic corrosion is a highly destructive phenomenon that severely impacts the structure of electrodes at negative potentials, specifically during electrocatalytic reduction reactions, such as CO2RR, that run at relatively high overpotential. This may undermine the stability of such electrodes in (future) commercial electrolyzers, as cathodically induced dissolution leads to consumption of the catalyst and furthermore, both dissolution as well as electrocrystallization phenomena result in preferential types of sites being produced, which may not necessarily be the most catalytically active sites for the reaction of interest as different facets generally exhibit different catalytic performance.[44] On

the other hand, leaving aside the stability aspect, cathodic corrosion may also lead to a surface site distribution that is actually beneficial for catalysis.[45] We note that this study was conducted in highly concentrated alkaline solution to accelerate cathodic corrosion, and that surface changes are expected to be less severe if electrolytes with lower cation concentrations are employed.

References

[1] Kevin J Warner and Glenn A Jones. The climate-independent need for renewable energy in the 21st century. *Energies*, 10(8):1197, 2017.

[2] Etosha R. Cave, Joseph H. Montoya, Kendra P. Kuhl, David N. Abram, Toru Hatsukade, Chuan Shi, Christopher Hahn, Jens K. Norskov, and Thomas F. Jaramillo. Electrochemical CO2 reduction on Au surfaces: mechanistic aspects regarding the formation of major and minor products. *Physical Chemistry Chemical Physics*, 19(24):15856–15863, 2017.

[3] Qi Lu, Jonathan Rosen, Yang Zhou, Gregory S Hutchings, Yannick C Kimmel, Jingguang G Chen, and Feng Jiao. A selective and efficient electrocatalyst for carbon dioxide reduction. *Nature communications*, 5:3242, 2014.

[4] Masashi Azuma, Kazuhito Hashimoto, Masahiro Hiramoto, Masahiro Watanabe, and Tadayoshi Sakata. Electrochemical reduction of carbon dioxide on various metal electrodes in low-temperature aqueous KHCO3 media. *Journal of the Electrochemical Society*, 137(6):1772–1778, 1990.

[5] Xiaoquan Min and Matthew W. Kanan. Pd-catalyzed electrohydrogenation of carbon dioxide to formate: High mass activity at low overpotential and identification of the deactivation pathway. *Journal of the American Chemical Society*, 137(14):4701–4708, 2015.

[6] Cao-Thang Dinh, Thomas Burdyny, Md Golam Kibria, Ali Seifitokaldani, Christine M. Gabardo, F. Pelayo García de Arquer, Amirreza Kiani, Jonathan P. Edwards, Phil De Luna, Oleksandr S. Bushuyev, Chengqin Zou, Rafael Quintero-Bermudez, Yuanjie Pang, David Sinton, and Edward H. Sargent. CO2 electroreduction to ethylene via hydroxide-mediated copper catalysis at an abrupt interface. *Science*, 360(6390):783–787, 2018.

[7] Christina W. Li, Jim Ciston, and Matthew W. Kanan. Electroreduction of carbon monoxide to liquid fuel on oxide-derived nanocrystalline copper. *Nature*, 508(7497):504–507, 2014.

[8] Sumit Verma, Byoungsu Kim, Huei-Ru "Molly" Jhong, Sichao Ma, and Paul J. A. Kenis. A gross-margin model for defining technoeconomic benchmarks in the electroreduction of CO2. *ChemSusChem*, 9(15):1972–1979, 2016.

[9] Alexei I. Yanson, Paramaconi Rodriguez, Nuria Garcia-Araez, Rik V. Mom, Frans D. Tichelaar, and Marc T. M. Koper. Cathodic corrosion: A quick, clean, and versatile method for the synthesis of metallic nanoparticles. *Angewandte Chemie International Edition*, 50(28):6346–6350, 2011.

[10] Nakkiran Arulmozhi, Derek Esau, Ram P. Lamsal, Diane Beauchemin, and Gregory Jerkiewicz. Structural transformation of monocrystalline platinum electrodes upon electro-oxidation and electro-dissolution. *ACS Catalysis*, 8(7):6426–6439, 2018.

[11] Thomas J. P. Hersbach, Ian T. McCrum, Dimitra Anastasiadou, Rianne Wever, Federico Calle-Vallejo, and Marc T. M. Koper. Alkali metal cation effects in structuring Pt, Rh, and Au surfaces through cathodic corrosion. *ACS Applied Materials & Interfaces*, 10(45):39363–39379, 2018.

[12] Thomas J. P. Hersbach, Alexei I. Yanson, and Marc T. M. Koper. Anisotropic etching of platinum electrodes at the onset of cathodic corrosion. *Nature Communications*, 7:12653, 2016.

[13] Matthew Jouny, Wesley Luc, and Feng Jiao. General techno-economic analysis of CO2 electrolysis systems. *Industrial & Engineering Chemistry Research*, 57(6):2165–2177, 2018.

[14] Xiong Peng, Stavros G. Karakalos, and William E. Mustain. Preferentially oriented Ag nanocrystals with extremely high activity and faradaic efficiency for CO2 electrochemical reduction to CO. *ACS Applied Materials & Interfaces*, 10(2):1734–1742, 2018.

[15] A. Hamelin. Cyclic voltammetry at gold single-crystal surfaces. Part 1. Behaviour at low-index faces. *Journal of Electroanalytical Chemistry*, 407(1):1–11, 1996.

[16] A. Hamelin and A. M. Martins. Cyclic voltammetry at gold single-crystal surfaces. Part 2. Behaviour of high-index faces. *Journal of Electroanalytical Chemistry*, 407(1):13–21, 1996.

[17] S. Štrbac, R. R. Adžć, and A. Hamelin. Oxide formation on gold single crystal stepped surfaces. *Journal of Electroanalytical Chemistry and Interfacial Electrochemistry*, 249(1):291–310, 1988.

[18] Enrique Herrero, Lisa J. Buller, and Héctor D. Abruña. Underpotential deposition at single crystal surfaces of Au, Pt, Ag and other materials. *Chemical Reviews*, 101(7):1897–1930, 2001.

[19] Ludwig A. Kibler. *Preparation and characterization of noble metal single crystal electrode surfaces*. International Society of Electrochemistry, 2003.

[20] Thomas J. P. Hersbach, Vladislav A. Mints, Federico Calle-Vallejo, Alexei I. Yanson, and Marc T. M. Koper. Anisotropic etching of rhodium and gold as the onset of nanoparticle formation by cathodic corrosion. *Faraday Discussions*, 193(0):207–222, 2016.

[21] Jonnathan Medina-Ramos, Weiwei Zhang, Kichul Yoon, Peng Bai, Ashwin Chemburkar, Wenjie Tang, Abderrahman Atifi, Sang Soo Lee, Timothy T. Fister, Brian J. Ingram, Joel Rosenthal, Matthew Neurock, Adri C. T. van Duin, and Paul Fenter. Cathodic corrosion at the bismuth–ionic liquid electrolyte interface under conditions for CO2 reduction. *Chemistry of Materials*, 30(7):2362–2373, 2018.

[22] Nakkiran Arulmozhi and Gregory Jerkiewicz. Design and development of instrumentations for the preparation of platinum single crystals for electrochemistry and electrocatalysis research. Part 1: Semi-automated crystal growth. *Electrocatalysis*, 7(6):507–518, 2016.

[23] J. Clavilier, R. Faure, G. Guinet, and R. Durand. Preparation of monocrystalline Pt microelectrodes and electrochemical study of the plane surfaces cut in the direction of the {111} and {110} planes. *Journal of Electroanalytical Chemistry and Interfacial Electrochemistry*, 107(1):205–209, 1980.

[24] R. Kaischew and B. Mutaftschiew. Uber die elektrolytische keimbildung des quecksilbers. *Electrochimica Acta*, 10(7):643–650, 1965.

[25] Nakkiran Arulmozhi, Derek Esau, Julia van Drunen, and Gregory Jerkiewicz. Design and development of instrumentations for the preparation of platinum single crystals for electrochemistry and electrocatalysis research. Part 3: Final treatment, electrochemical measurements, and recommended laboratory practices. *Electrocatalysis*, 9(1):113–123, 2018.

[26] S. Trasatti and O. A. Petrii. Real surface area measurements in electrochemistry. *Journal of Electroanalytical Chemistry*, 327(1):353–376, 1992.

[27] T. L. Einstein. *Equilibrium Shape of Crystals*, book section 5, pages 215–264. Elsevier, Boston, 2015.

[28] Serhiy Cherevko, Aleksandar R. Zeradjanin, Gareth P. Keeley, and Karl J. J. Mayrhofer. A comparative study on gold and platinum dissolution in acidic and alkaline media. *Journal of The Electrochemical Society*, 161(12):H822–H830, 2014.

[29] Maximilian Schalenbach, Olga Kasian, Marc Ledendecker, Florian D. Speck, Andrea M. Mingers, Karl J. J. Mayrhofer, and Serhiy Cherevko. The electrochemical dissolution of noble metals in alkaline media. *Electrocatalysis*, 9(2):153–161, 2018.

[30] Jicheng Feng, Dong Chen, Ahmad S. Sediq, Stefan Romeijn, Frans D. Tichelaar, Wim Jiskoot, Jun Yang, and Marc T. M. Koper. Cathodic corrosion of a bulk wire to nonaggregated functional nanocrystals and nanoalloys. *ACS Applied Materials & Interfaces*, 10(11):9532–9540, 2018.

[31] S. C. Abrahams, A. P. Ginsberg, and K. Knox. Transition metal-hydrogen compounds. II. The crystal and molecular structure of potassium rhenium hydride, K2ReH9. *Inorganic Chemistry*, 3(4):558–567, 1964.

[32] Stewart F. Parker. Spectroscopy and bonding in ternary metal hydride complexes—potential hydrogen storage media. *Coordination Chemistry Reviews*, 254(3):215–234, 2010.

[33] A. I. Yanson, P. V. Antonov, P. Rodriguez, and M. T. M. Koper. Influence of the electrolyte concentration on the size and shape of platinum nanoparticles synthesized by cathodic corrosion. *Electrochimica Acta*, 112:913–918, 2013.

[34] Michelle L. Personick and Chad A. Mirkin. Making sense of the mayhem behind shape control in the synthesis of gold nanoparticles. *Journal of the American Chemical Society*, 135(49):18238–18247, 2013.

[35] Ali Seifitokaldani, Christine M. Gabardo, Thomas Burdyny, Cao-Thang Dinh, Jonathan P. Edwards, Md Golam Kibria, Oleksandr S. Bushuyev, Shana O. Kelley, David Sinton, and Edward H. Sargent. Hydronium-induced switching between CO2 electroreduction pathways. *Journal of the American Chemical Society*, 140(11):3833–3837, 2018.

[36] Christine M. Gabardo, Ali Seifitokaldani, Jonathan P. Edwards, Cao-Thang Dinh, Thomas Burdyny, Md Golam Kibria, Colin P. O'Brien, Edward H. Sargent, and David Sinton. Combined high alkalinity and pressurization enable efficient CO2 electroreduction to CO. *Energy & Environmental Science*, 11(9):2531–2539, 2018.

[37] Stephanie Nitopi, Erlend Bertheussen, Soren B. Scott, Xinyan Liu, Albert K. Engstfeld, Sebastian Horch, Brian Seger, Ifan E. L. Stephens, Karen Chan, Christopher Hahn, Jens K. Nørskov, Thomas F. Jaramillo, and Ib Chorkendorff. Progress and perspectives of electrochemical CO2 reduction on copper in aqueous electrolyte. *Chemical Reviews*, 119(12):7610–7672, 2019.

[38] N. Gupta, M. Gattrell, and B. MacDougall. Calculation for the cathode surface concentrations in the electrochemical reduction of CO2 in KHCO3 solutions. *Journal of Applied Electrochemistry*, 36(2):161–172, 2006.

[39] Hideaki Kita, Hiroshi Nakajima, and Kimitaka Hayashi. Electrochemical oxidation of CO on Au in alkaline solution. *Journal of Electroanalytical Chemistry and Interfacial Electrochemistry*, 190(1):141–156, 1985.

[40] Paramaconi Rodriguez, Nuria Garcia-Araez, Andrey Koverga, Stefan Frank, and Marc T. M. Koper. CO electroxidation on gold in alkaline media: A combined electrochemical, spectroscopic, and DFT study. *Langmuir*, 26(14):12425–12432, 2010.

[41] Flemming Besenbacher, Erik Lægsgaard, and Ivan Stensgaard. Fast-scanning STM studies. *Materials Today*, 8(5):26–30, 2005.

[42] Jun Wang, Monica McEntee, Wenjie Tang, Matthew Neurock, Arthur P. Baddorf, Petro Maksymovych, and John T. Yates. Formation, migration, and reactivity of Au-CO complexes on gold surfaces. *Journal of the American Chemical Society*, 138(5):1518–1526, 2016.

[43] Nakkiran Arulmozhi, Thomas J. P. Hersbach, and Marc T. M. Koper. Nanoscale morphological evolution of monocrystalline Pt surfaces during cathodic corrosion. *Proceedings of the National Academy of Sciences*, page 202017086, 2020.

[44] Stefano Mezzavilla, Sebastian Horch, Ifan E. L. Stephens, Brian Seger, and Ib Chorkendorff. Structure sensitivity in the electrocatalytic reduction of CO2 with gold catalysts. *Angewandte Chemie*, 131(12):3814–3818, 2019.

[45] Matteo Duca, Paramaconi Rodriguez, Alexei I. Yanson, and Marc T. M. Koper. Selective electrocatalysis on platinum nanoparticles with preferential (100) orientation prepared by cathodic corrosion. *Topics in Catalysis*, 57(1):255–264, 2014.